The Astrophysical Journal, 897:87 (10pp), 2020 July 1 https://doi.org/10.3847/1538-4357/ab93b6

Using Stereoscopic Observations of Cometary Plasma Tails to Infer Solar Wind Speed

Long Cheng[1,2,3], Quanhao Zhang[1,2,3], Yuming Wang[1,2,3], Xiaolei Li[1,2,3], and Rui Liu[1,2,3]
[1] CAS Key Laboratory of Geospace Environment, School of Earth and Space Sciences, University of Science and Technology of China, Hefei 230026, People's Republic of China; zhangqh@ustc.edu.cn, ymwang@ustc.edu.cn
[2] CAS Center for Excellence in Comparative Planetology, University of Science and Technology of China, Hefei 230026, People's Republic of China
[3] Mengcheng National Geophysical Observatory, University of Science and Technology of China, Mengcheng 233500, People's Republic of China
Received 2020 January 16; revised 2020 May 4; accepted 2020 May 15; published 2020 July 6

Abstract

Detection of the solar wind speed near the Sun is significant in understanding the heating and acceleration of the solar wind. Cometary plasma tails have long been used as natural probes for solar wind speed; previous solar wind speed estimates via plasma tails, however, were based on comet images from a single viewpoint, and the projection effect may influence the result. Using stereoscopic observations from the Solar Terrestrial Relations Observatory and the Solar and Heliospheric Observatory, we three-dimensionally reconstruct the plasma tails of three comets C/2012 S1 (ISON), C/2010 E6, and C/2011 W3 (Lovejoy) and infer the ambient solar wind speed. The first comet is located between 3.5 and 6 solar radii (Rs) away from the Sun at high latitudes; the estimated solar wind speed is about 300–500 km s^{-1}. The second comet is located within 10 Rs and about 20° away from the ecliptic; the estimated solar wind speed is about 200–320 km s^{-1}. The third comet is also located at low latitudes but farther (>20 Rs) away from the Sun; the estimated solar wind speed is about 100–600 km s^{-1}. For comets near the ecliptic, our results are close to those predicted by MHD models, whereas for the comet at high latitudes, the deviation between our estimate and the model results is notable. This consistency and difference could be used to constrain and improve solar wind models. We will seek opportunities to apply the method to comet 322P, whose tail may sweep the Parker Solar Probe.

Unified Astronomy Thesaurus concepts: Solar wind (1534); Comet tails (274)

1. Introduction

The solar wind is a continuous streamer of plasma emanating from the solar corona to the interplanetary space, which may invade and disturb the Earth's magnetic field and upper atmosphere (Abbo et al. 2016; Cranmer et al. 2017). The measurement of the solar wind speed near the Sun is significant in understanding the heating and the acceleration of the solar wind in the corona and the inner heliosphere (Hansteen & Leer 1995). Traditionally, the solar wind speed was measured from either in situ or remote sensing observations. In situ observations have been performed by a series of satellites such as the Ulysses (Wenzel et al. 1992), Advanced Composition Explorer (Stone et al. 1998), and Wind (Acuña et al. 1995; Ogilvie & Desch 1997), but most of them are far from the Sun. Remote sensing observations, such as the Ultraviolet Coronagraph Spectrometer (Kohl et al. 1995) on board the Solar and Heliospheric Observatory (SOHO; Domingo et al. 1995), have enabled us to estimate the evolution of solar wind speed in the corona by using a Doppler dimming technique (Withbroe et al. 1982; Noci et al. 1987). Moreover, measuring interplanetary radio scintillation (IPS) from ground-based observatories enables the exploration of the solar wind speed in the interplanetary space with the cadence of a few hours (Kojima et al. 1998; Manoharan 2012; Imamura et al. 2014). Recently, Cho et al. (2018) applied Fourier filtering to SOHO/LASCO C3 data and provided estimations of the two-dimensional solar wind speed within 6–26 Rs over weekly to yearly periods.

Comets have been studied as natural probes of the solar wind since the mid-20th century (Biermann 1951; Belton & Brandt 1966; Brandt & Heise 1970). Through analyzing the properties of comet plasma tails, Biermann (1951) predicted the flow of charged particles from the Sun with high velocity, which was named as the solar wind later (Parker 1963). The most striking structures formed by the interaction of a comet and the solar wind are the comet tails, including the dust tail and the plasma tail. The dust tail appears as a besom of destruction sweeping the sky; it is shaped by both the solar radiation pressure and solar gravity. The plasma tail is a production of cometary charged particles picked up by the solar wind; it shines through the fluorescence of the particles and orientates close to the anti-solar direction. The changes in the morphology and the motion of comet tails could be studied to investigate the physical parameters of the corona and inner heliosphere (Bemporad et al. 2005; Downs et al. 2013; McCauley et al. 2013; Raymond et al. 2014, 2018). Especially, the sungrazer comets, whose perihelion is within Mercury's orbit (Jones et al. 2018), are natural explorers in probing the solar magnetic field and the solar wind acceleration region (Bryans & Pesnell 2012, 2016; Schrijver et al. 2012; Giordano et al. 2015). For example, the disconnection of comet plasma tails is helpful to detect the rapid change of the heliospheric magnetic field and the solar wind speed (Jia et al. 2007; Vourlidas et al. 2007; Buffington et al. 2008).

By investigating the motion of the plasmoids moving along the solar radial direction observed by the Solar Mass Ejection Imager (Eyles et al. 2003), Buffington et al. (2008) also estimated the solar wind speed. Clover et al. (2010) generalized this method to determine the solar wind speeds over large areas of space with the observations from HI-1 on board the Solar Terrestrial Relations Observatory (STEREO; Howard et al. 2008). Belton & Brandt (1966) proposed that the aberration angle of the comet plasma tail from the anti-solar direction is closely related to the solar wind speed. Based on this aberration angle, they estimated the local solar wind speed at the position of the comet at different distances and latitudes from a large

number of comet observations. It is noteworthy that these previous studies were based on comet observations in a single viewpoint so that they were more or less affected by the projection effect. The stereoscopic observations by STEREO and SOHO make it possible to reduce the projection effects. In this paper, we use STEREO and SOHO observations from different viewpoints to reconstruct the three-dimensional (3D) comet plasma tail and derive the solar wind speed from the angle between the comet plasma tail, the solar wind velocity, and the comet velocity. In Section 2, we will describe the observations of the comets and 3D reconstructions of the plasma tails. In Section 3, we will introduce our method of calculating the solar wind speed from comet plasma tails and display the results. In Section 4, we will give a brief conclusion and discussion of our method and results.

2. Observations and Measurements

The STEREO mission consists of two spacecraft, STEREO-A and STEREO-B, which orbit at ∼1.001 and ∼0.988 au, respectively, and provide viewpoints of the Sun that are different from the Earth (Kaiser et al. 2007). The COR2 detectors of STEREO provide white-light images of the corona covering a field-of-view (FOV) from 2.5 to 15 Rs (Howard et al. 2008), while HI-1 detectors observe the inner heliosphere with the range of about 15–84 Rs (Eyles et al. 2009). The typical cadence of each instrument is 15 and 40 minutes, respectively. SOHO is in orbit around the First Lagrangian Point (L1) and have two coronagraphs used to observe the extended solar corona; one is the C2 detector imaging from 1.5 to 6 Rs, the other is the C3 detector imaging from 3.5 to 30 Rs, with the same cadence of 12 minutes but different time stamps (Domingo et al. 1995).

We select three comets whose plasma tails were clearly observed among STEREO-A, STEREO-B, and SOHO, as shown in Figure 1. Figure 1(a) shows the comet C/2012 S1 (ISON) in COR2-B and COR2-A on 2013 November 28 at 15:54 UT. This comet came into the FOV of both COR2 detectors with a bright and broad dust tail on 2013 November 28 at 04:24 UT. Due to the extremely harsh near-Sun environment, comet ISON showed a straight plasma tail separated from the dust tail from 14:54 UT until it came into COR2 occulter disk, as shown by the red arrow in the images. Figure 1(c) shows the comet C/2010 E6 in COR2-B and COR2-A detectors on 2010 March 12 at 17:24 UT. This comet had a fainter plasma tail than the comet C/2012 S1 in COR2 FOV, which is also marked by red arrows in the right panel of Figure 1(c). Figure 1(e) shows the comet C/2011 W3 (Lovejoy) in HI-1B and HI-1A FOVs on 2011 December 18 at 18:09 UT. Both the dust tail and plasma tail of this comet were quite clear in the HI-1 FOVs for about three days. During the periods when these three comets appeared in STEREO or SOHO images, there was no large solar wind transient, e.g., coronal mass ejection (CME), propagating nearby, so these comet events are suitable for studying the solar wind variance in the quiet inner heliosphere.

We use the scc_measure procedure in Solar SoftWare (SSW) under an Interactive Data Language (IDL) environment to three-dimensionally reconstruct the comet plasma tail. First, after inputting a pair of images at the same time, e.g., COR2-A and COR2-B, we select a point representing a certain position in the comet plasma tail in, e.g., COR2-A. The program then displays a line in the corresponding COR2-B image, which is just the line-of-sight direction along with the selected point from the COR2-A image. We then select a point on this line in the COR2-B image, which corresponds to the same position in the plasma tail. Using this procedure, the 3D coordinates of this position in the plasma tail can be calculated and output as radial distance in solar radii (Rs) and the heliographic longitude and latitude. Repeating this procedure for different points in the plasma tail, we may fit those points with a 3D line across the comet nucleus to reconstruct the straight plasma tail and derive the direction of the plasma tail, $\hat{\boldsymbol{t}}$, as shown in Figures 1(b), (d), and (f). The fitting uncertainty of the direction $\hat{\boldsymbol{t}}$ would cause uncertainty in the calculation of the angle ϵ in Equation (4), which will be introduced in the next section, and eventually result in the uncertainty of the solar wind speed, w, in Equation (2).

Applying the scc_measure procedure to the plasma tails at different times, we could get the evolution of the 3D position and direction of the plasma tails. In this study, we choose the time 14:54 to 16:54 on 2013 November 28 for the comet C/2012 S1 (ISON) in COR2, 14:54 to 17:39 on 2010 March 12 for the comet C/2012 S1 C/2010 E6 in COR2, 2011 December 17–18 in HI-1 and sets of times during 2011 December 16–17 in C3 and COR2-B for the comet C/2013 (Lovejoy). Figure 1(b) shows an example of the 3D sketches of comet C/2012 S1 (ISON) in the Helio-Centric-Inertial (HCI) coordinate system as reconstructed by the scc_measure routine using COR2 images. The comet approached the Sun from ∼5.5 to ∼3.5 Rs as time increased, with a plasma tail lagging behind a few degrees to the radial direction from the Sun. According to the comet velocity and the 3D reconstructed plasma tails, we then calculate the local solar wind speed at the position of the comet, which will be introduced in the next section.

3. Analysis and Results

When a comet approaches the Sun, the photoionization of the neutral molecules around the comet nucleus will result in charged particles, which form the comet plasma tail (Saito et al. 1994). The charged particles in the plasma tail are picked up by the solar wind and eventually move with the solar wind plasma flow. Therefore, the charged particles should move along the solar wind direction in the HCI coordinate system. The charged particles at different times form the comet plasma tail. Due to the motion of the comet, the plasma in the tail has a velocity relative to the comet

$$\boldsymbol{t} = \boldsymbol{w} - \boldsymbol{v}, \tag{1}$$

where $\boldsymbol{w}$ is the solar wind velocity and $\boldsymbol{v}$ is the comet orbital velocity (Krishna Swamy 2010). The direction of $\boldsymbol{t}$ is just along the direction of the plasma tail. The comet orbital position and velocity could be obtained by using comet ephemeris from the Minor Planet and Comet Ephemeris Service, as listed in Table 1. Besides, it could be a useful test of the 3D reconstruction method to determine the nucleus coordinates from the application of the ssc_measure procedure and from the comet ephemeris. We first use the wcs_get_pixel procedure in SSW to get the projection points of the nucleus coordinate of the comet ISON on 2013 December 28 14:54 from the comet ephemeris on COR2-A and COR2-B images. Then we use scc_measure to locate the point in 3D space by the projection pixels. The nucleus coordinate determined from scc_measure is (5.5941 Rs, 98°.4544, −65°.1978) in distance, longitude, and

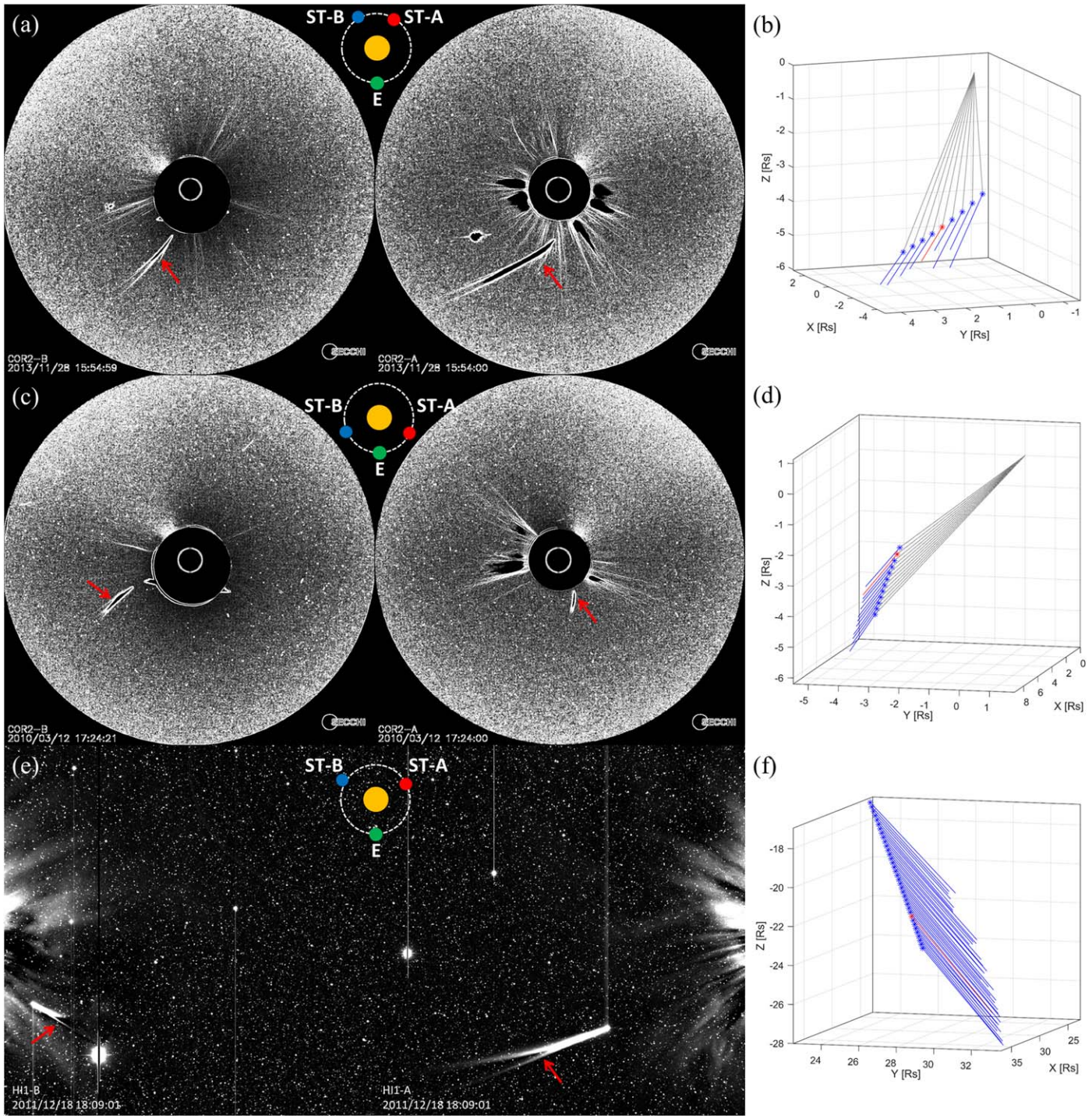

Figure 1. Observations and 3D reconstructions of the plasma tails of comets C/2012 S1 (ISON), C/2010 E6, and C/2011 W3 (Lovejoy) from top to bottom. (a) Observation of comet C/2012 S1 on 2013 November 28 15:54 UT in COR2-B and COR2-A. (c) Observation of comet C/2010 E6 on 2010 March 12 17:24 UT in COR2-B and COR2-A. (e) Observation of comet C/2011 W3 on 2011 December 18 at 18:09 UT in HI-1B and HI-1A. The plasma tails are pointed out by the red arrows in each image. Panels (b), (d), and (f) show the 3D reconstructions of the plasma tails of these three comets in the Helio-Centric-Inertial (HCI) coordinate system with the time interval of 15 minutes for COR2 and 40 minutes for HI-1. The dashed lines represent the Sun–comet lines; the blue asterisks represent the comet nucleus; the red line represents the tail reconstructed from the image shown in the corresponding left panels; the blue lines represent the reconstructed plasma tails at other times.

latitude; it is in good agreement with the same 3D point obtained from the comet ephemeris, which is (5.5937 Rs, 98°.4566, −65°.1948). Hence, we consider the scc_measure procedure in SSW as a valid 3D reconstruction tool.

Figure 2 shows a schematic cartoon of a reconstructed comet plasma tail in 3D space. The blue arrow shows the plasma tail vector; the red arrow shows the vector of the solar wind speed, which is just along the radial direction, $\hat{\boldsymbol{r}}$, if we ignoring the negligible solar wind azimuthal component (Marsch 2018); the brown arrow depicts the comet velocity vector. One way of attempting to calculate the solar wind velocity, $\boldsymbol{w}$, is to use Equation (1) theoretically. However, $\boldsymbol{t}$ in Equation (1)

Table 1
The Values of the Comet Positions and Velocities in the HCI Coordinate System and the Aberration Angles with Uncertainties

Time (UT)	Comet Position[a]			Comet Velocity[a]			Aberration Angle (deg)	Observations
	Radial Distance (Rs)	Longitude (deg)	Latitude (deg)	Vx (km s^{-1})	Vy (km s^{-1})	Vz (km s^{-1})		
				C/2012 S1 (ISON)				
2013 Nov 28 14:54	5.59	98.5	−65.2	−136.7	−175.6	136.6	16.03 ± 0.30	COR2-A&B
2013 Nov 28 15:09	5.35	104.0	−66.2	−136.0	−178.9	144.2	16.03 ± 0.30	COR2-A&B
2013 Nov 28 15:24	5.11	110.6	−67.1	−134.9	−182.4	152.5	17.83 ± 0.29	COR2-A&B
2013 Nov 28 15:39	4.86	118.2	−67.8	−133.4	−185.8	161.6	20.41 ± 0.25	COR2-A&B
2013 Nov 28 15:54	4.62	127.1	−68.1	−131.2	−189.3	171.8	21.42 ± 0.30	COR2-A&B
2013 Nov 28 16:09	4.38	136.9	−67.8	−128.1	−192.7	183.1	23.27 ± 0.24	COR2-A&B
2013 Nov 28 16:24	4.15	147.4	−66.8	−124.0	−195.9	195.7	25.94 ± 0.17	COR2-A&B
2013 Nov 28 16:39	3.91	157.8	−65.0	−118.5	−198.7	209.6	28.14 ± 0.28	COR2-A&B
2013 Nov 28 16:54	3.69	167.7	−62.3	−111.3	−200.9	224.9	31.50 ± 0.35	COR2-A&B
				C/2010 E6				
2010 Mar 12 14:54	9.17	337.1	−26.6	−136.7	−175.6	136.6	8.01 ± 0.48	COR2-A&B
2010 Mar 12 15:09	8.92	336.5	−26.4	−136.0	−178.9	144.2	8.57 ± 0.16	COR2-A&B
2010 Mar 12 15:24	8.66	335.9	−26.1	−134.9	−182.4	152.5	8.26 ± 0.35	COR2-A&B
2010 Mar 12 15:39	8.41	335.3	−25.8	−133.4	−185.8	161.6	8.82 ± 0.23	COR2-A&B
2010 Mar 12 15:54	8.15	334.6	−25.4	−131.2	−189.3	171.8	8.98 ± 0.31	COR2-A&B
2010 Mar 12 16:09	7.88	333.9	−25.1	−128.1	−192.7	183.1	9.28 ± 0.52	COR2-A&B
2010 Mar 12 16:24	7.62	333.2	−24.7	−124.0	−195.9	195.7	10.00 ± 0.28	COR2-A&B
2010 Mar 12 16:39	7.34	332.4	−24.3	−118.5	−198.7	209.6	10.05 ± 0.61	COR2-A&B
2010 Mar 12 16:54	7.06	331.6	−23.8	−111.3	−200.9	224.9	10.18 ± 0.33	COR2-A&B
2010 Mar 12 17:09	6.79	330.7	−23.3	−136.7	−175.6	136.6	11.39 ± 0.70	COR2-A&B
2010 Mar 12 17:24	6.50	329.7	−22.8	−136.0	−178.9	144.2	12.26 ± 0.60	COR2-A&B
2010 Mar 12 17:39	6.21	328.6	−22.2	−134.9	−182.4	152.5	12.66 ± 0.55	COR2-A&B
				C/2011 W3 (Lovejoy)				
2011 Dec 16 21:54	20.85	50.2	−23.8	91.4	69.8	−71.2	7.18 ± 3.12	C3 + COR2-B
2011 Dec 16 23:54	22.19	49.5	−24.4	88.9	66.8	−69.5	7.35 ± 4.49	C3 + COR2-B
2011 Dec 17 00:54	22.84	49.1	−24.6	87.8	65.4	−68.6	5.88 ± 3.30	C3 + COR2-B
2011 Dec 17 01:54	23.49	48.8	−24.8	86.7	64.2	−67.9	5.66 ± 2.74	C3 + COR2-B
2011 Dec 17 03:54	24.76	48.2	−25.3	84.6	61.9	−66.4	5.65 ± 3.42	C3 + COR2-B
2011 Dec 17 04:54	25.38	47.9	−25.4	83.7	60.8	−65.8	6.00 ± 3.63	C3 + COR2-B
2011 Dec 17 05:54	26.00	47.6	−25.6	82.8	59.8	−65.1	6.26 ± 4.31	C3 + COR2-B
2011 Dec 17 12:09	29.89	46.1	−26.6	77.6	54.7	−61.5	6.46 ± 5.83	HI-1A&B
2011 Dec 17 12:49	30.28	46.0	−26.7	77.3	53.5	−61.1	5.20 ± 4.29	HI-1A&B
2011 Dec 17 13:29	30.65	45.9	−26.8	76.8	53.1	−60.8	6.96 ± 5.37	HI-1A&B
2011 Dec 17 14:09	31.03	45.7	−26.9	76.3	53.4	−60.5	6.97 ± 3.00	HI-1A&B
2011 Dec 17 14:49	31.40	45.6	−27.0	75.8	52.9	−60.2	5.97 ± 5.55	HI-1A&B
2011 Dec 17 15:29	31.78	45.5	−27.0	75.5	52.1	−59.9	7.42 ± 6.70	HI-1A&B
2011 Dec 17 16:09	32.15	45.4	−27.1	75.2	51.4	−59.6	6.60 ± 4.92	HI-1A&B
2011 Dec 17 16:49	32.51	45.2	−27.2	74.8	51.0	−59.3	6.28 ± 6.34	HI-1A&B
2011 Dec 17 17:29	32.88	45.1	−27.3	74.2	51.3	−59.1	6.68 ± 3.61	HI-1A&B
2011 Dec 17 18:09	33.24	45.0	−27.3	73.9	50.9	−58.8	7.05 ± 3.29	HI-1A&B
2011 Dec 17 18:49	33.61	44.9	−27.4	73.6	49.8	−58.4	7.37 ± 2.71	HI-1A&B
2011 Dec 17 19:29	33.96	44.8	−27.5	73.3	49.5	−58.2	6.46 ± 4.48	HI-1A&B
2011 Dec 17 20:09	34.32	44.7	−27.5	72.8	49.8	−58.0	5.65 ± 4.99	HI-1A&B

Table 1
(Continued)

Time (UT)	Comet Position[a]			Comet Velocity[a]			Aberration Angle (deg)	Observations
	Radial Distance (Rs)	Longitude (deg)	Latitude (deg)	Vx (km s^{-1})	Vy (km s^{-1})	Vz (km s^{-1})		
				C/2012 S1 (ISON)				
2011 Dec 17 20:49	34.68	44.6	−27.6	72.4	49.5	−57.7	5.98 ± 4.02	HI-1A&B
2011 Dec 17 21:29	35.03	44.5	−27.7	72.2	48.8	−57.4	7.88 ± 3.34	HI-1A&B
2011 Dec 17 22:09	35.39	44.4	−27.7	71.9	48.1	−57.2	7.36 ± 6.92	HI-1A&B
2011 Dec 17 22:49	35.74	44.3	−27.8	71.6	47.8	−56.9	7.54 ± 6.29	HI-1A&B
2011 Dec 17 23:29	36.09	44.2	−27.8	71.1	48.2	−56.8	7.07 ± 5.26	HI-1A&B
2011 Dec 18 00:09	36.65	44.0	−27.9	70.6	47.7	−56.4	5.71 ± 1.83	HI-1A&B
2011 Dec 18 00:49	37.00	44.0	−28.0	70.3	47.0	−56.1	5.23 ± 3.21	HI-1A&B
2011 Dec 18 01:29	37.34	43.9	−28.1	70.1	46.4	−55.8	5.16 ± 2.66	HI-1A&B
2011 Dec 18 02:09	37.68	43.8	−28.1	69.8	46.1	−55.6	5.28 ± 2.64	HI-1A&B
2011 Dec 18 02:49	38.02	43.7	−28.2	69.4	46.5	−55.5	4.64 ± 2.58	HI-1A&B
2011 Dec 18 03:29	38.36	43.6	−28.2	69.1	46.3	−55.3	4.41 ± 3.25	HI-1A&B
2011 Dec 18 04:09	38.70	43.5	−28.3	68.9	45.3	−55.0	4.87 ± 3.21	HI-1A&B
2011 Dec 18 04:49	39.04	43.4	−28.3	68.7	45.0	−54.8	5.14 ± 2.18	HI-1A&B
2011 Dec 18 05:29	39.37	43.4	−28.4	68.3	45.5	−54.7	4.89 ± 2.96	HI-1A&B
2011 Dec 18 06:09	39.71	43.3	−28.4	68.0	45.2	−54.5	5.19 ± 2.18	HI-1A&B
2011 Dec 18 06:49	40.04	43.2	−28.5	67.8	44.6	−54.2	5.24 ± 4.30	HI-1A&B
2011 Dec 18 07:29	40.37	43.1	−28.5	67.6	44.0	−54.0	4.98 ± 2.37	HI-1A&B
2011 Dec 18 08:09	40.70	43.0	−28.6	67.3	43.7	−53.8	5.16 ± 2.22	HI-1A&B
2011 Dec 18 08:49	41.03	43.0	−28.6	66.9	44.2	−53.7	4.86 ± 1.96	HI-1A&B
2011 Dec 18 09:29	41.36	42.9	−28.6	66.7	44.0	−53.5	5.33 ± 1.98	HI-1A&B
2011 Dec 18 10:09	41.68	42.8	−28.7	66.6	43.1	−53.2	4.85 ± 2.13	HI-1A&B
2011 Dec 18 10:49	42.00	42.8	−28.7	66.3	42.8	−53.1	5.44 ± 3.48	HI-1A&B
2011 Dec 18 11:29	42.33	42.7	−28.8	66.0	43.3	−53.0	4.75 ± 1.77	HI-1A&B
2011 Dec 18 12:09	42.65	42.6	−28.8	65.7	43.1	−52.8	4.69 ± 2.86	HI-1A&B
2011 Dec 18 12:49	42.97	42.5	−28.9	65.6	42.5	−52.6	5.22 ± 2.90	HI-1A&B
2011 Dec 18 13:29	43.29	42.5	−28.9	65.4	42.0	−52.4	4.95 ± 1.95	HI-1A&B
2011 Dec 18 14:09	43.61	42.4	−28.9	65.2	41.8	−52.2	5.09 ± 2.83	HI-1A&B
2011 Dec 18 14:49	43.93	42.3	−29.0	64.8	42.3	−52.1	5.25 ± 3.85	HI-1A&B
2011 Dec 18 15:29	44.25	42.3	−29.0	64.6	42.1	−51.9	5.02 ± 5.41	HI-1A&B
2011 Dec 18 16:09	44.56	42.2	−29.0	64.5	41.2	−51.7	4.93 ± 3.76	HI-1A&B
2011 Dec 18 16:49	44.87	42.1	−29.1	64.3	41.0	−51.5	5.36 ± 4.12	HI-1A&B
2011 Dec 18 17:29	45.19	42.1	−29.1	64.0	41.5	−51.5	4.87 ± 3.13	HI-1A&B
2011 Dec 18 18:09	45.50	42.0	−29.2	63.8	41.3	−51.3	5.57 ± 3.61	HI-1A&B
2011 Dec 18 18:49	45.81	42.0	−29.2	63.6	40.8	−51.1	4.99 ± 5.10	HI-1A&B
2011 Dec 18 19:29	46.12	41.9	−29.2	63.5	40.2	−50.9	5.67 ± 4.03	HI-1A&B
2011 Dec 18 20:09	46.43	41.8	−29.3	63.3	40.0	−50.8	5.27 ± 4.45	HI-1A&B
2011 Dec 18 20:49	46.74	41.8	−29.3	63.0	40.6	−50.7	6.07 ± 6.77	HI-1A&B
2011 Dec 18 21:29	47.05	41.7	−29.3	62.8	40.4	−50.6	5.90 ± 5.17	HI-1A&B
2011 Dec 18 22:09	47.35	41.7	−29.4	62.7	39.5	−50.3	5.43 ± 4.67	HI-1A&B
2011 Dec 18 22:49	47.66	41.6	−29.4	62.5	39.4	−50.2	5.57 ± 4.20	HI-1A&B
2011 Dec 18 23:29	47.96	41.6	−29.4	62.2	39.9	−50.1	6.03 ± 5.29	HI-1A&B

Note.
[a] Coordinates in the HCI coordinate system.

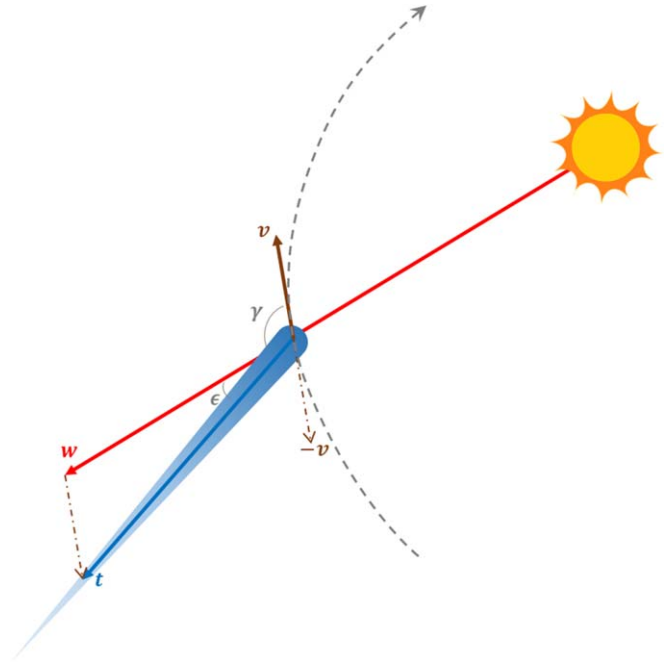

Figure 2. Sketch of comet plasma tail in the comet obit plane. The gray dashed line represents the comet orbit; the golden arrow represents the comet speed vector; the blue arrow represents the comet plasma tail's vector; the red arrow represents the solar wind speed vector. γ is the angle between the solar wind direction and the comet speed direction; ϵ is the aberration angle between the plasma tail to the solar wind direction.

essentially means the relative plasma speed to the comet, which is hard to obtain from the images directly and be used for the calculation of the solar wind velocity, $\boldsymbol{w}$; we can only achieve the direction of the plasma tail, $\hat{\boldsymbol{t}}$. Since these three speed vectors form the triangular principle of vector addition, we could calculate the local solar wind speed at the position of the comet by the sine theorem

$$w = v\frac{\sin(\gamma + \epsilon)}{\sin\epsilon}, \tag{2}$$

where γ is the angle between the comet speed and the radial solar wind speed, ϵ is the angle between the direction of the comet plasma tail and the solar wind speed vector, which is the aberration angle. These two angles are determined by:

$$\gamma = \arccos\hat{\boldsymbol{v}} \cdot \hat{\boldsymbol{r}} \tag{3}$$

$$\epsilon = \arccos\hat{\boldsymbol{t}} \cdot \hat{\boldsymbol{r}}. \tag{4}$$

With the method introduced above, we estimate the local solar wind speed at positions of the comets described in Section 2 from the comet position and velocity and the aberration angle. All the values of the comet positions, the comet velocities, and the aberration angles with uncertainties obtained in this work are listed in Table 1. Figure 3 shows the results from the comet C/2012 S1 (ISON), including the solar wind speed (the red line in top panel), the heliocentric distance (middle panel), the longitude and the latitude of the comet in the HCI coordinate system (bottom panel). Our estimate suggests that the solar wind speed at the position of the comet decreased from ∼500 to ∼300 km^{-1}, when the comet C/2012 S1 (ISON) came closer to the Sun from ∼5.5 Rs to ∼3.5 Rs with time increasing. During this period, the comet's latitude was around −65° with a little change, while its longitude changed by about 70°.

We try to compare our results to some empirical or MHD models of the solar wind. We run the MHD simulations on the Community Coordinated Modeling Center (CCMC) website. In this case, considering the heliocentric distance within 10 Rs, we run the Magnetohydrodynamic Algorithm outside a Sphere (MAS) model for the comparison. The MAS code is a 3D coronal model that depicts the solar wind parameters within 20 Rs, it integrates the time-dependent resistive thermodynamic magnetohydrodynamic equations in 3D spherical coordinates and is used extensively in modeling coronal structures (Linker et al. 1999). The MAS model on CCMC has two types: the polytropic MHD model with simple energy physics that can describe coronal structure qualitatively, and the thermodynamic MHD model that can further describe the temperature quantitatively. We input the period of Carrington Rotation (CR) 2144 covering the day of 2013 November 28 into these two models and calculate the solar wind speed at the position of the comet ISON. We find that the solar wind speeds predicted by the MAS show similar trends but are much smaller than those derived by our method. The solar wind speed by the MAS model only ranges between 200 and 300 $\mathrm{km\,s^{-1}}$. It is noteworthy that MHD models hardly simulate the solar wind very accurately in the high latitude region, due to the lack of accurate observation of the photospheric magnetograms in the polar regions. In particular, the comparison between the MAS simulation and in situ measurements by Ulysses shows its underestimation of the solar wind speed at middle to high latitudes, and most of the other MHD models are just limited to ±60° in latitude (Riley et al. 2012; Jian et al. 2016). This should be the reason for the obvious deviation between the solar wind speeds estimated by our method and those predicted by the MAS model.

The second comet, C/2010 E6, appeared in both COR2 images after 23:24 on 2010 March 11. Its plasma tail was clear since 14:54 on 2010 March 12, especially in COR2-B image. There were also no large solar wind transients propagating nearby when this comet could be observed in COR2 FOV. Figures 4 shows the solar wind speed (the red line in top panel), the heliocentric distance (middle panel), and the longitude and the latitude in the HCI coordinate system (bottom panel). As for comet C/2010 E6, it came closer to the Sun from ∼9 Rs to ∼6 Rs during this period; its longitudes experience several degrees variance around 332° and the latitudes vary several degrees around −25°, which implies a low latitude region. The solar wind speeds increase from ∼200 to ∼300 $\mathrm{km\,s^{-1}}$ as the heliocentric distance increasing from ∼6 Rs to ∼9 Rs. We also compare our results with the two MAS models of CR 2094 covering the day of 2010 March 12 in this region. As shown in the top panel of Figure 4, the solar wind speeds estimated from our method are generally consistent with those from MAS thermodynamic and polytropic models. Actually, the results from two MAS models are different in detail; the solar wind speeds from the MAS thermodynamic model are ∼150 $\mathrm{km\,s^{-1}}$ greater than those from the MAS polytropic model. Our results are between those two ranges and are closer to the result of the MAS thermodynamic model.

The third comet we choose is the comet C/2011 W3 (Lovejoy), which is observed by LASCO C3, STEREO COR2, and HI-1. The comet plasma could not only be clearly recognized in both C3 and COR2-B images during 2011 December 16–17, but also in both HI-1A and HI-2B images on December 17–18. The estimated solar wind speeds are shown

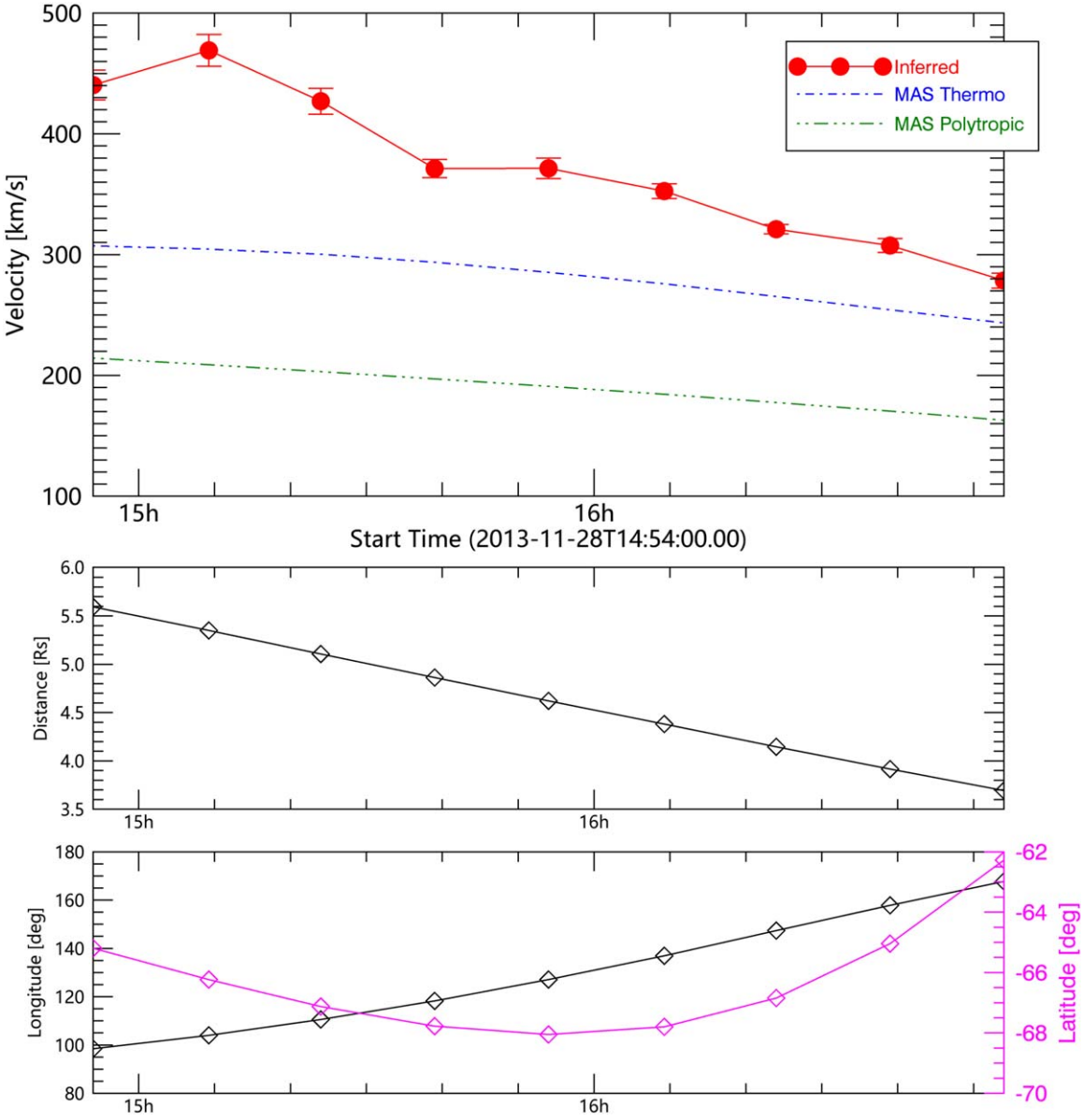

Figure 3. Variation of the solar wind speed, the comet–Sun distance, the longitude and the latitude of comet C/2012 S1 (ISON). Top panel: variation of the solar wind speed calculated by our method (red) and that from the Magnetohydrodynamic Algorithm outside a Sphere (MAS) thermodynamic (blue) and polytropic (green) model. Middle panel:variation of the comet–Sun distance. Bottom panel: variation of the longitude (black) and the latitude (magenta) of the comet in the HCI coordinate system.

in Figure 5. During this period, comet C/2011 W3 (Lovejoy) gradually moved from ∼20 Rs to ∼50 Rs. Due to the larger distance from the Sun, the comet velocity is near radial, so that the change of the longitudes (∼46°) and latitudes (∼27°) is small. Although the error bars are large due to the large uncertainty of the measured aberration angle, we may still infer that the solar wind speed at the position of the comet varies around 300 km s^{-1} and tends to decrease with time.

For this comet, due to the large comet–Sun distance (>20 Rs), we choose two heliospheric MHD models, the heliospheric tomography with IPS data (Jackson et al. 1997) and a CME model (ENLIL; Odstrcil et al. 1996; Odstrcil 2003) on CCMC, for the comparison. The 3D reconstruction technique by the heliospheric tomography incorporates a kinematic solar wind model and tomographically fit this to ground-based IPS data provided by Solar Terrestrial Environment Laboratory (STELab). ENLIL is a time-dependent 3D MHD model of the heliosphere and solves equations for plasma mass, momentum and energy density, and magnetic field, using a Flux-Corrected-Transport algorithm. We run these two heliospheric models on CCMC and achieve the solar wind parameters outside 20 Rs during CR 2118 covering the day of 2011 December 16–18. As shown by the blue and green lines in the top panel of Figure 5, the solar wind speeds from our method are generally consistent with the results from the two interplanetary models considering the large error bars. Different from the corona models, these heliospheric models are also constrained by the solar wind parameters measured at STEREO-A, STEREO-B, and the spacecraft near the Earth (e.g., WIND) besides the magnetogram of the solar photosphere. The results from the heliospheric models should be more valid and provide stronger support to our method.

In brief, the solar wind speeds from our method using observations of comet C/2010 E6 in COR2 and C/2011 W3

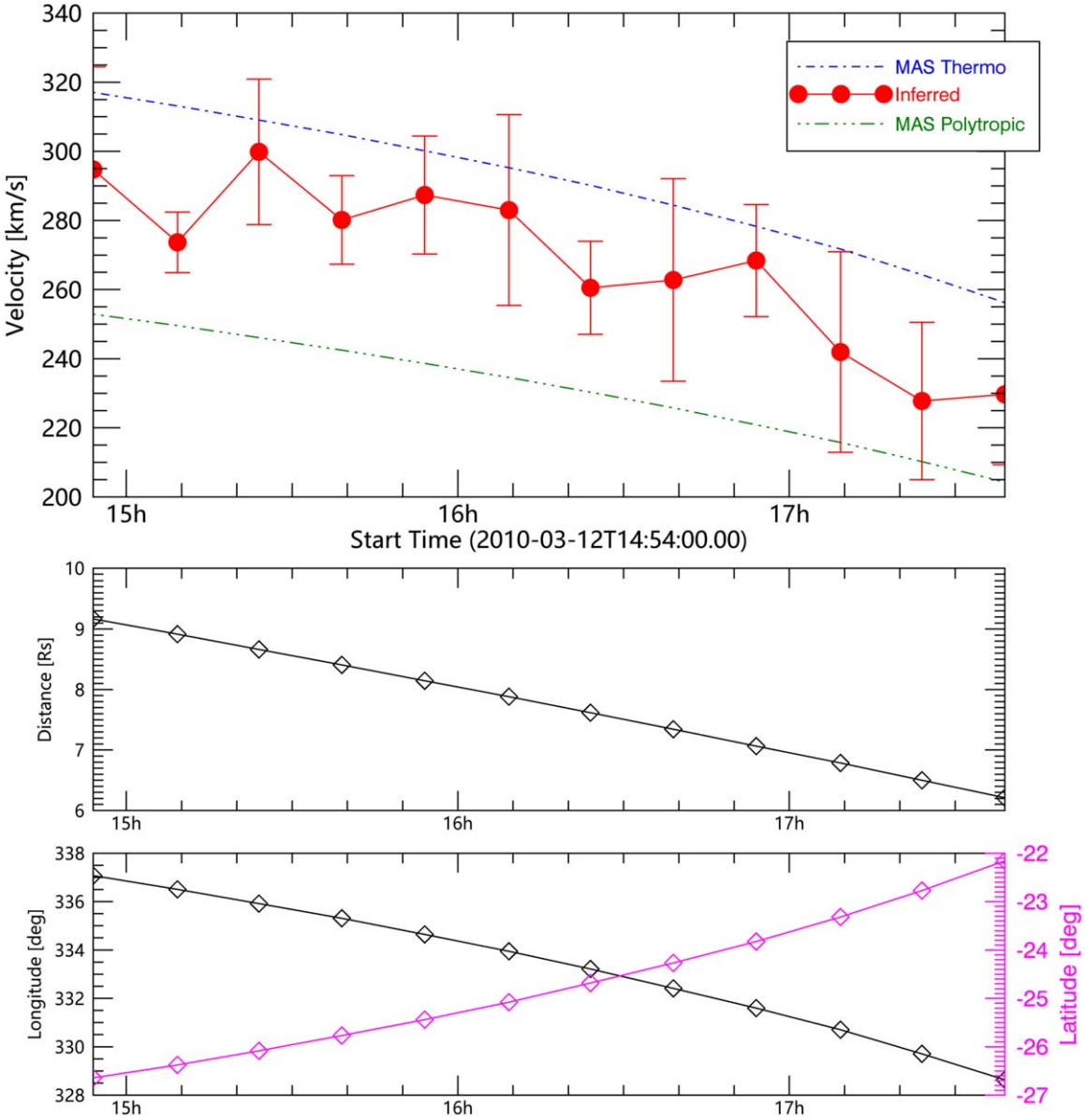

Figure 4. Variation of the solar wind speed, the comet–Sun distance, the longitude and the latitude of comet C/2010 E6. The panel arrangement is the same as Figure 3, but with comparison to the solar wind speed from the MAS thermodynamic (blue) and polytropic (green) model in the top panel additionally.

(Lovejoy) in HI-1 are consistent with those from the MHD models in the low and medium latitude regions of the interplanetary space. The deviations between the solar winds inferred from the plasma tail of comet C/2012 S1 and those from the MHD models are probably due to the invalid of those models in the high latitude regions.

4. Conclusions and Discussions

In this work, we use stereoscopic observations to reconstruct the 3D comet plasma tail and then estimate the solar wind speed by measuring the aberration of the plasma tail from the solar wind direction. Through using stereoscopic observations, the influence of the projection effects on the measurement of the comet plasma tail could be reduced. For the first comet, C/2012 S1 (ISON) in COR2, we find that the solar wind speed at the positions of the comet varied from ∼500 to ∼300 km s^{-1} when the comet approach the Sun from ∼5.5 to ∼3.5 Rs in the high latitude region of about −65°. As for the second comet, C/2010 E6, which is close to the ecliptic plane, the derived solar wind speed decreased from ∼300 km s^{-1} to ∼200 km s^{-1} with the distance decreasing from ∼9 to ∼6 Rs. Both of the cases clearly show the solar wind acceleration within this region. We also infer the solar wind near the comet C/2011 W3 (Lovejoy), which moved from ∼20 to ∼50 Rs, and near the ecliptic plane. The solar wind speed estimated from this comet is about 100–600 km s^{-1}, with significant uncertainties, which mainly come from the uncertainty in determining the small aberration angle between the solar wind direction and the plasma tail.

The comparison between the solar wind speeds estimated by our method and the empirical or MHD models for the comets at low latitudes shows great agreement. At the position of the comet C/2010 E6, our estimated solar wind speed is consistent with that from the MAS thermodynamic and polytropic models; concretely, it is between the profiles given by the two models, and closer to the thermodynamic model. The solar

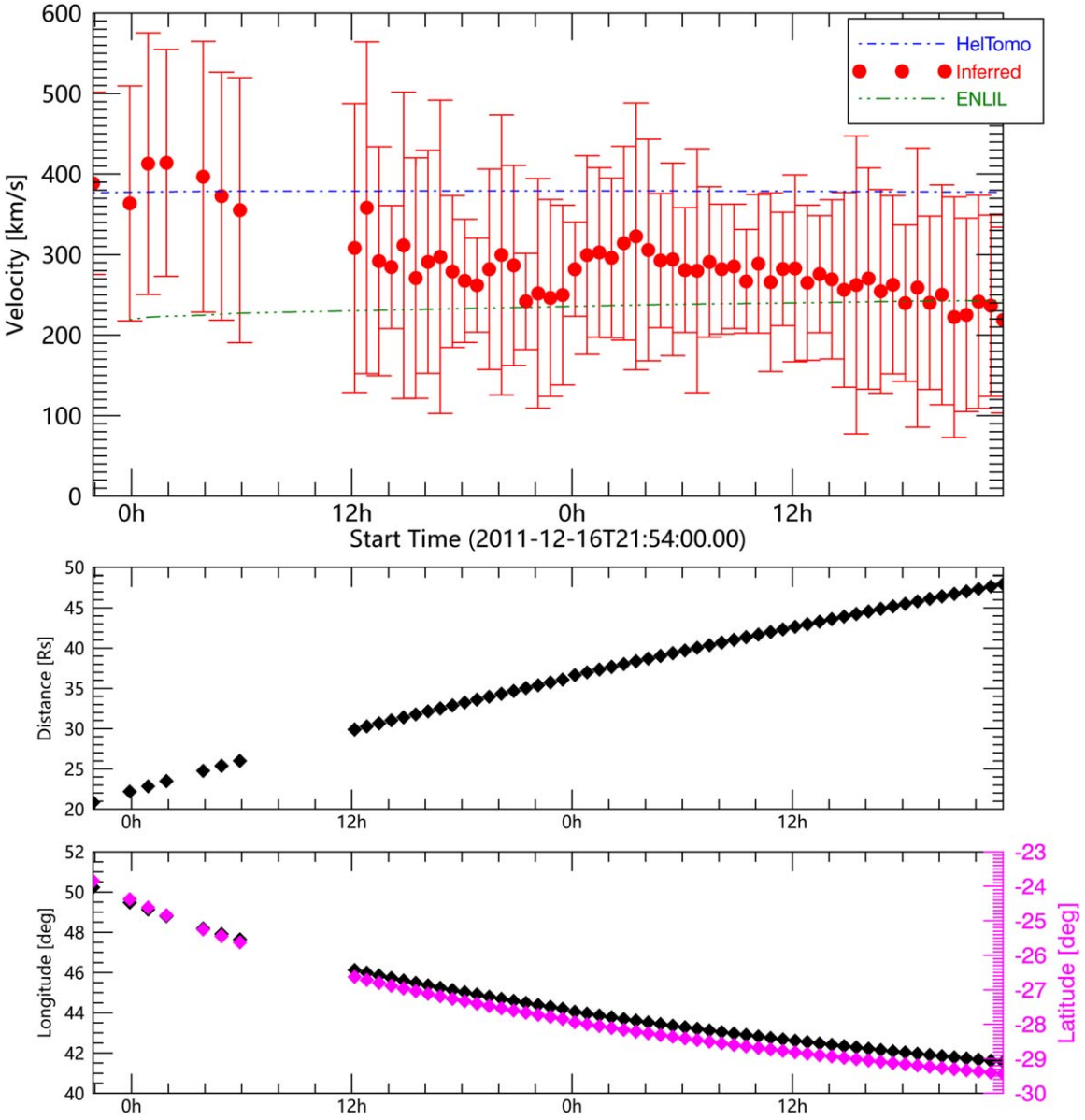

Figure 5. Variation of the solar wind speed, the comet–Sun distance, the longitude, and the latitude of the comet C/2011 W3 (Lovejoy). The panel arrangement is the same as Figure 3, but with comparison to the solar wind speed from the heliospheric tomography with IPS data (blue) and ENLIL model (green) in the top panel additionally. The first comet position is beyond the inner boundary (20Rs) of ENLIL model, so the solar wind speed from ENLIL (green) at this time is vacant.

wind speed deduced from the comet Lovejoy is also in good agreement with both the heliospheric tomography with IPS and the ENLIL model. However, the solar wind speeds estimated from the comet ISON, which are located at high latitudes, deviate from the MAS models. Such a deviation may come from the inadaptability of those MHD models in the high latitude regions. Nevertheless, through the agreement with the coronal MHD models using comets C/2010 E6 and C/2011 W3, our method is effective in the measurement of the solar wind speed in the low latitude, suggesting that the solar wind speed acquired by the method could be used to constrain and improve solar wind models.

We will seek opportunities to apply the method to comet 322P, whose tail is anticipated to sweep the Parker Solar Probe (PSP; Fox et al. 2016), and compare the inferred solar wind speed with in situ measurements. The database of comets in coronagraph images with clear plasma tails would be enriched by both more advanced image processing methods and more observations from new solar missions (e.g., PSP and Solar Orbiter). Applying this method to a sufficient amount of comets, we might be able to achieve a map of the 3D distribution of the solar wind speed in the inner heliosphere, especially where the in situ measurements by spacecraft are unavailable now. This will definitely advance our understanding of the corona heating and solar wind acceleration.

We thank the anonymous referee for the critical reviewing of the manuscript and constructive comments that helped to improve the paper. This research is supported by the Strategic Priority Program of CAS (XDB41000000 and XDA15017300), the grants from NSFC (Nos. 41804161, 41774178, and 41574165), and the fundamental research funds for the central universities. We thank the NASA's STEREO mission team for their public data available on several websites, including the STEREO Science Center (SSC) and STEREO FTP server. We also acknowledge the general tools in the IDL Solar SoftWare

(SSW) package contributed by the solar physics community. MHD simulations are run on the Community Coordinated Modeling Center (CCMC) website at NASA/GSFC. We appreciate all the modeling teams for providing their models at the CCMC.

ORCID iDs

Quanhao Zhang https://orcid.org/0000-0003-0565-3206
Yuming Wang https://orcid.org/0000-0002-8887-3919
Rui Liu https://orcid.org/0000-0003-4618-4979

References

Abbo, L., Ofman, L., Antiochos, S. K., et al. 2016, SSRv, 201, 55
Acuña, M. H., Ogilvie, K. W., Baker, D. N., et al. 1995, SSRv, 71, 5
Belton, M. J. S., & Brandt, J. C. 1966, ApJS, 13, 125
Bemporad, A., Poletto, G., Raymond, J. C., Biesecker, D. A., & Uzzo, M. 2008, ApJ, 620, 523
Biermann, L. 1951, ZA, 29, 274
Brandt, J. C., & Heise, J. 1970, ApJ, 159, 1057
Bryans, P., & Pesnell, W. D. 2012, ApJ, 760, 18
Bryans, P., & Pesnell, W. D. 2016, ApJ, 822, 77
Buffington, A., Bisi, M. M., Clover, J. M., et al. 2008, ApJ, 677, 798
Cho, I.-H., Moon, Y.-J., Nakariakov, V. M., et al. 2018, PhRvL, 121, 075101
Clover, J. M., Jackson, B. V., Buffington, A., Hick, P. P., & Bisi, M. M. 2010, ApJ, 713, 394
Cranmer, S. R., Gibson, S. E., & Riley, P. 2017, SSRv, 212, 1345
Domingo, V., Fleck, B., & Poland, A. I. 1995, SoPh, 162, 1
Downs, C., Linker, J. A., Mikić, Z., et al. 2013, Sci, 340, 1196
Eyles, C. J., Simnett, G. M., Cooke, M. P., et al. 2003, SoPh, 217, 319
Eyles, C. J., Harrison, R. A., Davis, C. J., et al. 2009, SoPh, 254, 387
Fox, N. J., Velli, M. C., Bale, S. D., et al. 2016, SSRv, 204, 7
Giordano, S., Raymond, J. C., Lamy, P., Uzzo, M., & Dobrzycka, D. 2015, ApJ, 798, 47
Hansteen, V. H., & Leer, E. 1995, JGR, 100, 21577
Howard, R. A., Moses, J. D., Vourlidas, A., et al. 2008, SSRv, 136, 67
Imamura, T., Tokumaru, M., Isobe, H., et al. 2014, ApJ, 788, 117
Jackson, B., Hick, P., Kojima, M., & Yokobe, A. 1997, PCE, 22, 425
Jia, Y. D., Combi, M. R., Hansen, K. C., & Gombosi, T. I. 2007, JGRA, 112, A05223
Jian, L. K., Macneice, P. J., Mays, M. L., Taktakishvili, A., & Sokolov, I. V. 2016, SpWea, 14, 592
Jones, G. H., Knight, M. M., Battams, K., et al. 2018, SSRv, 214, 20
Kaiser, M. L., Kucera, T. A., & Davila, J. M. 2007, SSRv, 136, 5
Kohl, J. L., Esser, R., Gardner, L. D., et al. 1995, SoPh, 162, 313
Kojima, M., Tokumaru, M., Watanabe, H., et al. 1998, JGR, 103, 1981
Krishna Swamy, K. S. 2010, Physics of Comets (Singapore: World Scientific)
Lamy, H., Pierrard, V., Maksimovic, M., & Lemaire, J. F. 2003, JGRA, 108, 1047
Linker, J. A., Mikić, Z., Biesecker, D. A., et al. 1999, JGR, 104, 9809
Manoharan, P. K. 2012, ApJ, 751, 128
Marsch, E. 2018, AnGeo, 36, 1607
McCauley, P. I., Saar, S. H., Raymond, J. C., Ko, Y. K., & Saint-Hilaire, P. 2013, ApJ, 768, 161
Noci, G., Kohl, J. L., & Withbroe, G. L. 1987, ApJ, 315, 706
Odstrcil, D. 2003, AdSpR, 32, 497
Odstrcil, D., Smith, Z., & Dryer, M. 1996, GeoRL, 23, 2521
Ogilvie, K. W., & Desch, M. D. 1997, AdSpR, 20, 559
Parker, E. N. 1963, Interplanetary Dynamical Processes (New York: Interscience Publishers), 1963
Raymond, J. C., Downs, C., Knight, M. M., et al. 2018, ApJ, 858, 19
Raymond, J. C., McCauley, P. I., Cranmer, S. R., & Downs, C. 2014, ApJ, 788, 152
Riley, P., Linker, J. A., Lionello, R., & Mikic, Z. 2012, JASTP, 83, 1
Saito, T., Kozuka, Y., Saito, K., & Minami, S. 1994, Dusty and Dirty Plasmas, Noise, and Chaos in Space and in the Laboratory (Berlin: Springer), 55
Schrijver, C. J., Brown, J. C., Battams, K., et al. 2012, Sci, 335, 324
Stone, E. C., Frandsen, A. M., Mewaldt, R. A., et al. 1998, SSRv, 86, 1
Vourlidas, A., Davis, C. J., Eyles, C. J., et al. 2007, ApJL, 668, L79
Wenzel, K. P., Marsden, R. G., Page, D. E., & Smith, E. J. 1992, A&AS, 92, 207
Withbroe, G. L., Kohl, J. L., Weiser, H., & Munro, R. H. 1982, SSRv, 33, 17